ADVANCED MATERIALS TECHNOLOGIES
www.advmattechnol.de

Oxygen Vacancies Modulation in $CoFe_2O_4$ via Two-Step Incorporation of Synergistic TiO_2/MXene and Carbon for Enhanced Acetone Sensing

Mengyuan Li, Ying Guo, Yuanyuan Guo, Hao Li, Paddy J. French, and Yao Wang**

Oxygen vacancy concentration in metal oxides is crucial to gas sensing performance. This study introduces a novel strategy of oxygen vacancies modulation on $CoFe_2O_4$, by two-step controllable incorporation of TiO_2@MXene and carbon. In the first step, MXene simultaneously acts as an incorporation agent and a titanium source to grow TiO_2 and regulate the oxygen vacancy concentration in $CoFe_2O_4$. The fabricated n-n heterojunctions of TiO_2/$CoFe_2O_4$ further induced a gradient distribution of oxygen vacancies through energy band bending. And a second step, combining glucose as a carbon source, further increases the oxygen vacancy concentration in $CoFe_2O_4$ by chemical reduction during a hydrothermal process, leading to the formation of a $CoFe_2O_4$-TiO_2@MXene-C nanostructured composite. Through controlling the glucose content, the ratio of Co^{3+} to Co^{2+} within the composite can be sequentially adjusted, which allows for the further regulation of oxygen vacancy concentration on the composite surface. The effectiveness of this two-step incorporation is demonstrated through enhanced acetone sensing performance, providing valuable insights into the fabrication of high-performance metal oxide-based gas sensors via controlled oxygen vacancy modulation.

1. Introduction

Volatile organic compounds (VOCs) originating from various sources, including industrial emissions, motor vehicle exhaust, and indoor air pollution, are a class of significant pollutants with detrimental effects on both environmental quality and human health.[1] Acetone (CH_3COCH_3), characterized by its flammability, toxicity, and low boiling point, also serves as a crucial biomarker for diabetes diagnosis.[2] Studies have indicated that healthy individuals exhaled acetone concentrations in breath ranging from 0.3 to 0.9 ppm, whereas diabetic patients present significantly elevated levels, ranging from 1.25 to 25 ppm.[3,4] Therefore, developing acetone gas sensors with high sensitivity and low detection limits is of great research significance for the application of diagnosing early diabetes through the detection of breath gases.

Among the acetone gas sensors, resistive gas sensors have harvested considerable attention due to their cost-effectiveness, compact size, and facile integration, offering advantages over techniques like spectrometry and chemiluminescence.[5,6] As resistive sensing materials, metal oxides are commonly used with good sensing properties, but exhibit limitations such as poor target selectivity and high operating temperatures. As is known to all, the oxygen vacancy structure has a key role in the gas sensing performance of metal oxides, which has been reported by many previous works. Conventional methods for oxygen vacancy regulation, such as elemental doping, high-temperature treatment, and plasma processing, all exhibit certain limitations.[7–9] For instance, achieving precise control over dopant concentration and depth distribution in elemental doping remains a significant challenge. Inadequate doping often leads to insufficient oxygen vacancy modulation, whereas excessive doping may introduce unintended impurities or secondary phases. These issues can result in undesirable sensor behaviors, including baseline drift, reduced selectivity, and compromised long-term stability. Plasma treatment, which primarily modifies the material surface (within a few nanometers), can generate oxygen vacancies confined to the superficial layers. Its effectiveness is constrained for thicker sensing materials or applications requiring bulk-phase regulation to optimize overall conductivity. Therefore, the development of a novel and efficient approach to modulate oxygen vacancies in metal oxides remains imperative.

M. Li, Y. Guo
State Key Laboratory of Chemical Resources Engineering
Beijing University of Chemical Technology
P. O. Box 98, Beijing 100029, P. R. China
E-mail: guoying@mail.buct.edu.cn
Y. Guo, H. Li, Y. Wang
Guangdong Provincial Key Laboratory of Optical Information Materials and Technology
Institute of Electronic Paper Displays
National Center for International Research on Green Optoelectronics
South China Academy of Advanced Optoelectronics
South China Normal University
Guangzhou 510006, P. R. China
E-mail: wangyao@m.scnu.edu.cn
P. J. French
BE Laboratory
EWI
Delft University of Technology
Delft 2628CD, The Netherlands
The ORCID identification number(s) for the author(s) of this article can be found under https://doi.org/10.1002/admt.202500901

DOI: 10.1002/admt.202500901

Recently, 2D materials, such as MXenes (e.g., $Ti_3C_2T_x$), have emerged as promising candidates for gaining better sensing performance due to their high conductivity, high specific surface area, abundant surface functional groups, and rapid electron transport capabilities.[10,11] However, pristine MXenes without any modification or complexation exhibit limitations as sensing materials for a wide range of gases/VOCs, including low bandgap, poor stability, aggregation tendency, and limited selectivity.[12] Therefore, much research is focused on the complexation of MXenes with metal oxides, leading to enhanced gases/VOCs sensing performance and the mitigation of the shortcomings of both sides. For instance, $Ti_3C_2T_x$ and its composites with different metal oxides, such as ZnO, TiO_2, Co_3O_4, $ZnFe_2O_4$, have demonstrated improved sensing results compared to their pristine counterparts.[13–16] Accordingly, the regulation of oxygen vacancy structure of metal oxide by MXene presents an effective strategy for modulating the electronic structure of materials, providing additional adsorption sites, and enhancing their sensing performance. Besides, it is worth noting that $Ti_3C_2T_x$ is also a titanium source to grow TiO_2 on its surface. By the in situ growth approach, the TiO_2-Fe_3O_4 heterojunction on the $Ti_3C_2T_x$ surface was reported by Huang et al., indicating significant gas sensing performance due to the large number of oxygen vacancies induced by charge transfer at the interface of TiO_2-Fe_2O_3 and thus promoting gas adsorption and surface reaction.[17] Therefore, the MXene phase transition process to TiO_2 synergistically modulates the concentration of the oxygen vacancies, which also reveals the key role of oxygen vacancy engineering in heterojunctions.[18–20]

Moreover, removing oxygen atoms from the material lattice by chemical reduction is another way to modulate oxygen vacancies. Recent studies have demonstrated that the reduction of metal oxides by carbon materials can introduce uniform oxygen vacancies through mild reactions.[21–23] For instance, Li et al. successfully synthesized oxygen-deficient ZrC composites through a combination of hydrothermal deposition and carbothermal reduction, utilizing sucrose as a carbon source.[24]

Hence, inspired by the above findings, $CoFe_2O_4$-TiO_2@MXene-C (CoTM-C) nanocomposites were prepared, and the oxygen vacancies were modulated through two-step incorporation of TiO_2@MXene and carbon on $CoFe_2O_4$. During the first incorporation process, MXene served as an incorporation agent, providing the abundant active sites and precisely regulating the concentration of oxygen vacancies at the interface between the metal oxide and MXene. The further in situ and partial oxidation of TiO_2 from MXene not only generates abundant oxygen-deficient active sites but also combines with $CoFe_2O_4$ to construct n-n heterojunctions. While the built-in electric field at the TiO_2/$CoFe_2O_4$ n-n heterointerface facilitates efficient charge transfer and a gradient distribution of oxygen vacancies through energy band bending. Additionally, the TiO_2 nanoparticles act as interlayer spacers, which extend the spacing of the $Ti_3C_2T_x$ layers to optimize the gas diffusion channels. And in the second incorporation, glucose was further introduced for carbothermal reduction to synergize carbon incorporation with Co^{3+}/Co^{2+} redox modulation, which achieves a fine optimization of the spatial distribution of oxygen vacancies and electronic states on $CoFe_2O_4$. The optimized gas sensor, by modulating the amount of glucose, shows excellent gas sensing performance, such as the response value for 100 ppm acetone at 185 °C is 52, and a response/recovery time is 17 s/54 s. Compared with $CoFe_2O_4$ alone, the response value is 2.3 times higher, and the response/recovery time is 35 s/100 s shorter. Not only that, the optimized gas sensor shows a stable response to low concentrations of acetone even at ppb level, which further verifies that the concentration modulation of oxygen vacancies of this sensor is effective for the enhancement of acetone sensing.

2. Results and Discussion

2.1. Material Characterization

As shown in schematic **Figure 1a**, in this study, multilayer $Ti_3C_2T_x$ MXene was first prepared by chemical etching of Ti_3AlC_2 precursor. Then, $CoFe_2O_4$ nanoparticles were grown on the surface of MXene by in situ hydrothermal method, and the $CoFe_2O_4$-TiO_2@MXene (abbreviated as CoTM) composites were successfully synthesized. As shown in schematic Figure 1b, in order to further optimize the material properties, a glucose-assisted hydrothermal approach was introduced in the subsequent steps to modify CoTM, and finally, glucose-modified $CoFe_2O_4$-TiO_2@MXene-C composites (abbreviated as CoTM-C) were obtained. Elemental analysis was conducted to determine the organic carbon contents of the four samples (CoTM-C). As shown in Figure S1 (Supporting Information), the results for CoTM-C1, CoTM-C2, CoTM-C3, and CoTM-C4 were 3.68%, 6.87%, 8.09%, and 13.47%, respectively, exhibiting an obvious gradient increase trend.

The physical phase composition and crystal structure of $CoFe_2O_4$, $Ti_3C_2T_x$, and CoTM-C series of composites were investigated systematically by X-ray powder diffractometer (XRD) characterization. The XRD patterns are shown in Figure 1c with a scanning range of 3°-80°. The patterns reveal that $CoFe_2O_4$ and CoTM-C series composites all have significant diffraction peaks at 2θ = 30.12°, 35.54°, 43.18°, 53.67°, 57.09°, and 62.73°, corresponding to (220), (311), (400), (422), (511), and (440) crystal planes of $CoFe_2O_4$, respectively. These peak positions match well with the standard XRD data for $CoFe_2O_4$ (JCPDS No. 22–1086), indicating that $CoFe_2O_4$ was successfully synthesized or contained in the composites.[25] At 2θ = 9.56°, the (002) diffraction peak of $Ti_3C_2T_x$ MXene appears, corresponding to its lamellar structure and reflecting the interlayer crystallographic spacing. It is noteworthy that the overall small angle shift of the (002) diffraction peak of MXene for the CoTM-C series composites compared to the pristine $Ti_3C_2T_x$ may be attributed to the intercalation of the $CoFe_2O_4$ nanoparticles, which results in an increase in the interlamellar spacing of the MXene layers.[26] In addition, the strongest diffraction peak (101) of TiO_2 is observed at 2θ = 25.28°, which is consistent with the standard XRD data of TiO_2 (JCPDS No. 21–1272), suggesting that partial oxidation of MXene in the CoTM-C series of composites occurs to form TiO_2. A broad (002) diffraction peak appears in the range of 2θ = 15°–30°, which indicates a degree of disorder in the crystal structure within the sample.

The surface functional groups of CoTM and CoTM-C series composites were characterized by Fourier transform infrared spectroscopy (FTIR). From the spectra in Figure 1d, it can be seen

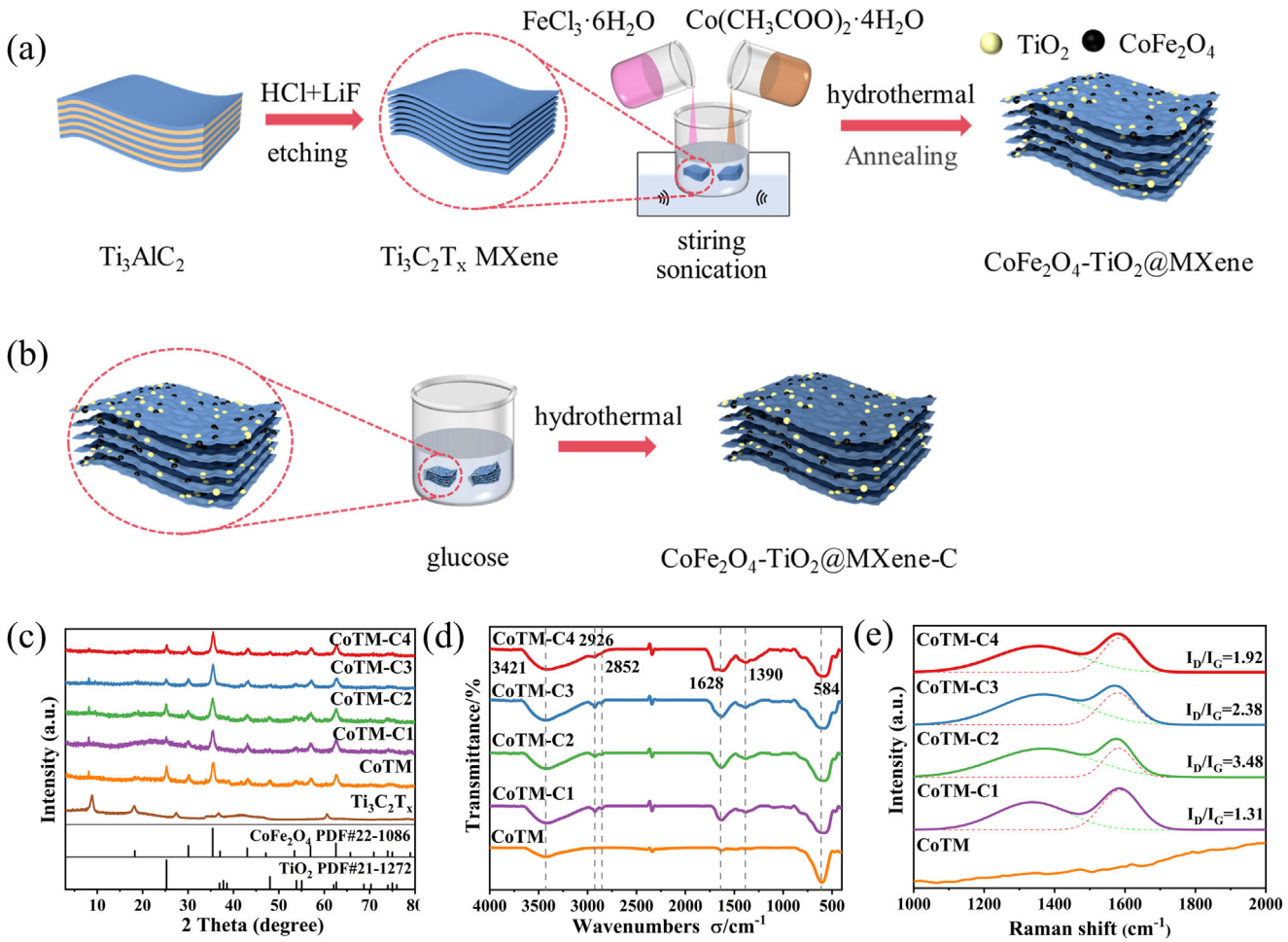

Figure 1. Schematic illustration of the synthetic procedure of CoTM a) and CoTM-C b); XRD patterns c) of $Ti_3C_2T_x$, CoTM, and CoTM-C series composites; FT-IR spectra d) and Raman plots e) of CoTM and CoTM-C series composites.

that the characteristic peaks at 3421 and 584 cm^{-1} occur in all the samples. The absorption peak at 3421 cm^{-1} is usually attributed to the stretching vibration of hydroxyl groups (—OH), which may originate from the water molecules adsorbed on the surface of the material or chemically bonded hydroxyl groups. It is noteworthy that the enhanced intensity of the absorption peak at 3421 cm^{-1} for the CoTM-C series samples compared to the no carbon-coated CoTM samples may be attributed to the contribution of hydroxyl groups in the carbon precursor (glucose) or the introduction of hydroxyl-containing species generated during the hydrothermal reaction. The characteristic absorption peak at 584 cm^{-1} can be attributed to the Co—O and Fe—O stretching vibrations, indicating the presence of $CoFe_2O_4$ in all samples.[27] The characteristic peaks of 2926, 2852, 1628, and 1390 cm^{-1} in the spectra only appear in CoTM-C series composites. The two weak absorption peaks at 2926 and 2852 cm^{-1} correspond to C—H stretching vibrations, which are usually associated with C—H bonds in long-chain alkanes or aldehyde groups.[28] This suggests that a small amount of aldehyde intermediates was generated during the hydrothermal process or that the aldehyde group in the glucose molecule was involved in the reaction. The absorption peak at 1628 cm^{-1} can be attributed to the C=C stretching vibration, suggesting that the glucose molecule underwent a dehydration condensation reaction and formed a conjugated double bond structure in the carbon skeleton during hydrothermal carbonization. The absorption peak at 1390 cm^{-1} is usually attributed to the bending vibration of C—OH, which is especially common in aromatic structures or phenolic compounds. It further suggests that glucose underwent partial aromatization during hydrothermal processes and formed functional groups similar to phenolic hydroxyl groups, further supporting the occurrence of the carbonation reaction.

In order to further assess the degree of graphitization of the samples, Raman spectroscopy was used for characterization. Usually, the D band (≈1320 cm^{-1}) corresponds to defects and disordered structures in the carbon material, while the G band (≈1590 cm^{-1}) reflects the ordered graphitized structure of sp^2 carbon.[29] As seen in Figure 1e, the D/G peak intensity ratios (I_D/I_G) of CoTM-C1, CoTM-C2, CoTM-C3, and CoTM-C4 were 1.31, 3.48, 2.38, and 1.92, respectively, with the highest degree of defects in CoTM-C2, while no obvious D/G peaks were observed for the sample without carbon coated (CoTM), probably due to the low carbon content, which makes it difficult to form an ordered carbon structure. When the carbon content is low

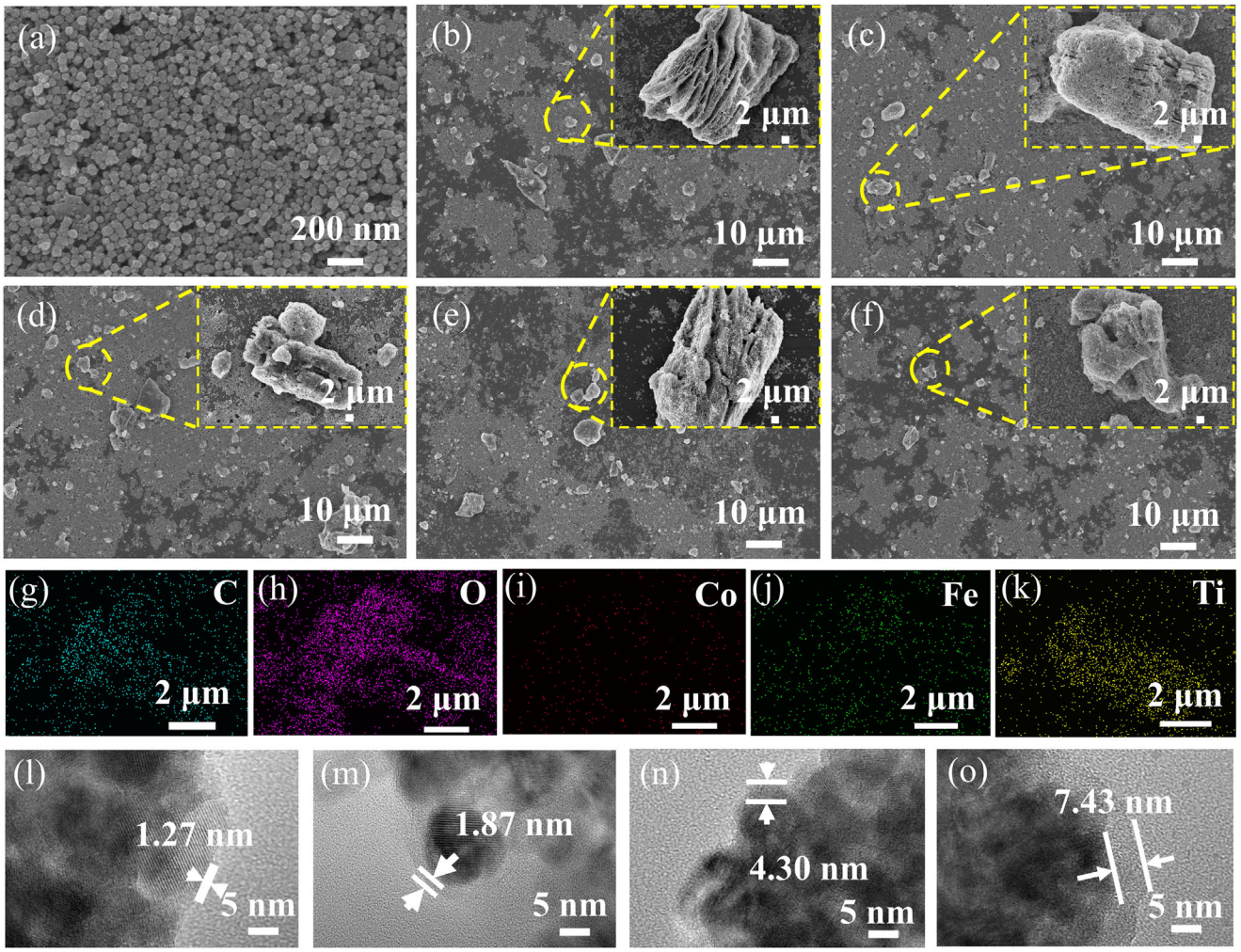

Figure 2. a–f) SEM images of $CoFe_2O_4$, CoTM, CoTM-C1, CoTM-C2, CoTM-C3, and CoTM-C4; g–k) elemental mapping of C, O, Co, Fe, and Ti for CoTM-C2; l–o) TEM images of CoTM-C1, CoTM-C2, CoTM-C3, and CoTM-C4.

(e.g., CoTM-C1 and CoTM-C2), the carbon atoms are difficult to self-assemble into a six-membered cyclic graphite flake layer but exist in the form of disordered carbon, which leads to an increase in defects and a rise in the I_D/I_G value. And with the increase of carbon content (e.g., CoTM-C3 and CoTM-C4), the connection between carbon atoms is more adequate, and it is easier to form a larger-scale ordered graphite layer. Hence, the defects are gradually reduced and the degree of graphitization is increased, which induces the decreased ratio of I_D/I_G. A moderate number of structural defects helps to optimize electron transport and active site distribution, which in turn enhances the gas-sensitive performance of gas sensors.

The morphologies of the $CoFe_2O_4$, CoTM, and CoTM-C composites were investigated using a combination of scanning electron microscopy (SEM) and energy spectroscopy (EDS) with elemental analysis. As illustrated in **Figure 2**a, the $CoFe_2O_4$ sample consists of uniform spherical nanoparticles with a diameter of ≈50 nm. From the SEM images (Figure 2b–f) of the composites, it can be seen that lamellar $Ti_3C_2T_x$ MXene is distributed on the surface. The local magnification images further reveal that the $CoFe_2O_4$ nanospheres are not only distributed on the surface of the MXene but are also partially intercalated between the layers of the MXene, which indicates the close contact between the layered MXene and the $CoFe_2O_4$ nanoparticles. As illustrated in Figure 2g–k, elemental mapping confirms the uniform distribution of all components in CoTM-C2, thereby the formation of optimal interfacial contacts.

In order to observe more directly the effect of the addition of a glucose carbon source on the microstructure of the CoTM-C series samples, the thickness of the coated carbon layer of the CoTM-C series samples was characterized using high resolution transmission electron microscopy (HRTEM). The HRTEM images revealed the glucose-derived carbon layer thickness in CoTM-C series, showing controlled growth with increasing carbon source. As shown in Figure 2l–o, it can be seen that the CoTM-C series composites are encapsulated by the carbon layer, although the carbon shells are difficult to keep completely homogeneous during the reaction process. And the thickness of the carbon layer increases with the gradual increase of glucose carbon source, which are 1.27, 1.87, 4.30, and 7.43 nm, respectively.

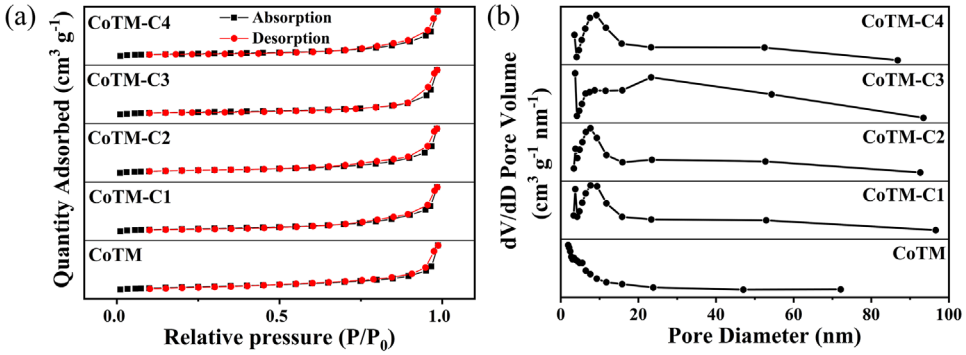

Figure 3. a) N_2 adsorption-desorption isotherms and b) pore size distribution curves of the composites of CoTM and CoTM-C.

It suggests that the thickness of the carbon layer coated on the surface of $CoFe_2O_4$-TiO_2@MXene can be effectively controlled by regulating the addition of glucose during the synthesis process. Thus, the carbon content of the composite and its structural properties can be regulated.

As shown in **Figure 3a**, the N_2 adsorption-desorption isotherms of CoTM-C composites are similar in shape, and the energy required for desorption is higher than that required for adsorption. The isotherms show H3-type hysteresis loops and belong to the type IV adsorption isotherms, indicating that the pore structures in the materials are mesoporous. From the pore size distribution graphs (Figure 3b), it can be observed that the pore sizes of the composites are all in the range of 15.5–16.1 nm, which has a relatively large pore size and is favorable for gas molecule transport. The specific surface area of the composites listed in **Table 1** shows that CoTM-C2 has the largest specific surface area of 52.5320 $m^2\ g^{-1}$. A larger specific surface area and pore size mean more active sites for oxygen adsorption, enabling the material to adsorb more gas molecules, which is an important factor affecting the gas-sensing performance. The specific surface area of the composites increases and then decreases as more carbon is added. This may be due to the fact that excess carbon blocks the pore structure of the material, which is not conducive to the diffusion of gas molecules and therefore reduces the reaction between the gas molecules and the sensing material.

X-ray photoelectron spectroscopy (XPS) was used to study the chemical composition and elemental surface valence states of the composites. **Figure 4a** shows the full-width scanning spectra of CoTM and CoTM-C composites, and the presence of five elemental peaks of C, Ti, Fe, Co, and O can be seen. Further analyzing the chemical states of every element, as shown in Figure 4b, the peaks of the Ti 2p spectra at 458.2 and 464.2 eV correspond to the Ti $2p_{3/2}$ and Ti $2p_{1/2}$ orbitals, respectively, indicating that Ti in the composites exists in the form of Ti^{4+}. Since XPS can only detect compositional information on solid surfaces at a depth of analysis within 10 nm, this suggests that the surface of MXene was oxidized to TiO_2. As shown in Figure 4c, the O 1s region can be decomposed into three peaks: adsorbed oxygen (O_C: 533.4 eV), oxygen vacancy (O_V: 531.6 eV), and lattice oxygen (O_L: 530.0 eV). Among the four peaks that appeared in the high-resolution spectra of Co 2p (Figure 4d), two peaks could be attributed to Co $2p_{3/2}$ and its satellite peaks (782.8 and 780.5 eV, respectively), while the other two peaks corresponded to Co $2p_{1/2}$ and its satellite peaks (798.0 and 796.5 eV, respectively).[30] The calculated contents from the integration areas of the adsorbed oxygen, oxygen vacancies, lattice oxygen, and Co^{2+} are shown in **Table 2**. It can be seen that the relative contents of oxygen vacancies and Co^{2+} vary in a consistent relationship. As the carbon content increases, the concentrations of Co^{2+} and O_V also increase, with the oxygen vacancy content of the CoTM-C series composites exhibiting the following sequence: CoTM-C2 > CoTM-C1 > CoTM-C3 > CoTM-C4. Notably, the sample CoTM-C2 has the highest concentration of Co^{2+} and Ov, followed by a decrease in the oxygen vacancy concentration along with the increased carbon content. On the one hand, because Co^{3+} is reduced by the hydrothermal process of glucose, which provides electrons to Co^{3+}, causing the oxidation state of Co^{3+} to be reduced. In order to fulfill the electron transfer and stoichiometric relationship of this reduction process, oxygen atoms in the crystal are released as oxygen ions, forming oxygen vacancies.[22] On the other hand, the larger ionic radius of Co^{2+} compared to Co^{3+} induces significant lattice distortion in $CoFe_2O_4$, elongating the Co—O bonds and reducing their binding energy. This strain destabilizes the oxygen coordination, lowers the energy barrier for oxygen vacancy formation, and promotes the creation of oxygen vacancies. This distortion reduces the stability of the crystal structure and makes the bonding of the oxygen atom with the surrounding ions weaker. In this unstable structural state, oxygen atoms are more likely to overcome the lattice bonding and detach from the lattice, resulting in the formation of oxygen vacancies. As for CoTM-C3 and CoTM-C4, when too much carbon content is added, it will block the MXene interlayer voids, which is unfavorable for electron transport. The above studies show that the chemical composition and surface state of CoTM-C series composites can be effectively regulated by controlling the addition of glucose, which in turn adjusts the gas sensing properties.

Table 1. BET surface areas and pore sizes of the CoTM-C composites.

Sample	BET Surface Area [$m^2\ g^{-1}$]	Pore Size [nm]
CoTM-C1	52.1758	17.2728
CoTM-C2	52.5320	17.9730
CoTM-C3	50.6347	23.6174
CoTM-C4	45.1087	19.5603

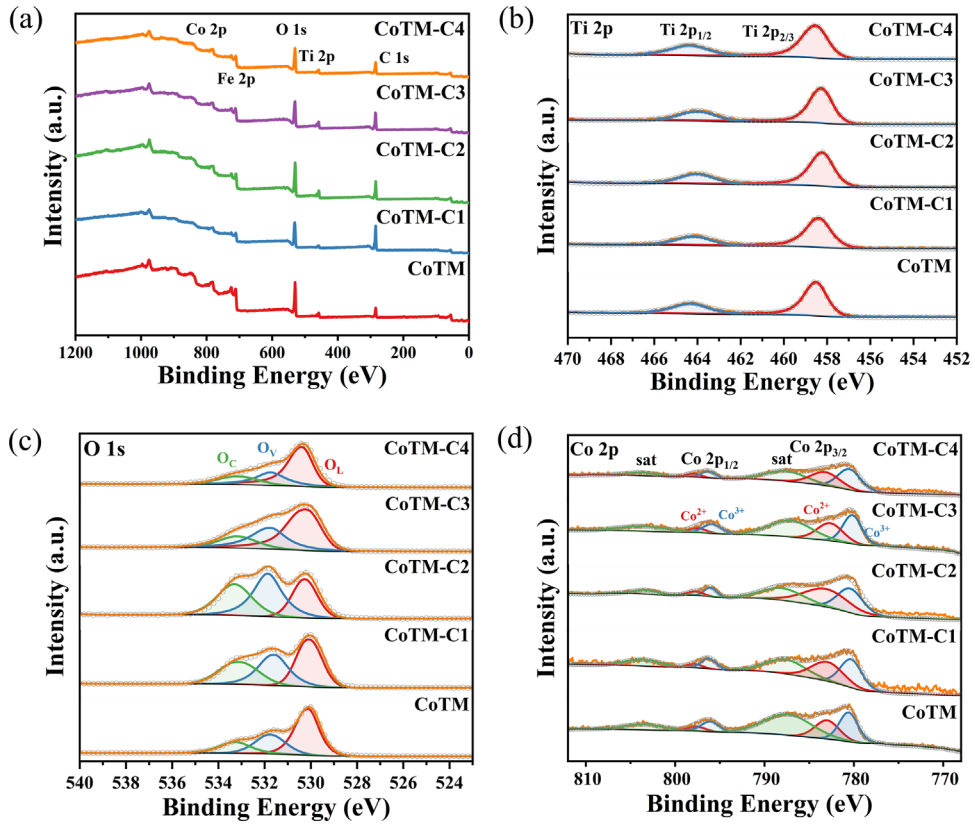

Figure 4. The full XPS survey spectra a) and the fitted XPS spectra of b)Ti 2p; c) O 1s; d) Co 2p for CoTM and CoTM-C composites.

2.2. Sensing Performance

In order to investigate the potential application of carbon coating treatment in gas sensitization, gas sensors based on CoTM-C composites were fabricated and systematically investigated regarding their gas sensing performance for acetone. In order to determine the optimum operating temperature of the sensor, **Figure** 5a shows the response (Ra/Rg) variation of the CoTM-C-based sensors to 100 ppm acetone at varied operating temperatures ranging from 155 to 245 °C. The experimental results show that the response value increases gradually with the increasing temperature and reaches the maximum value at 185 °C. Subsequently, the response value decreases with further increasing temperature. The whole change trend may be attributed to the fact that a suitable temperature helps the adsorption and reaction of acetone molecules on the sensor surface and increases the carrier concentration. However, when the temperature is too high, the microstructure of the sensing material may change, and the enhanced carrier scattering effect leads to a decrease in sensitivity. At the optimum operating temperature of 185 °C, the relationship between the response values of the samples with different carbon contents is CoTM-C2 > CoTM-C1 > CoTM-C3 > CoTM-C4. This may be attributed to the fact that the oxygen vacancy content on the surface of the CoTM-2 sample (32.80%) is higher than that of the other samples, which was mentioned in the XPS spectra (Figure 4c and Table 2). The oxygen vacancies provide more gas adsorption sites and act as an activator for the acetone molecules. In addition, the excellent BET-specific surface area and pore size of CoTM-C2 (Figure 3) also contributed significantly to the gas sensing performance. For comparison, the response (Ra/Rg) variation of the sensors of $CoFe_2O_4$, CoTM, $CoFe_2O_4$-C, and CoTM-C2 was tested to 100 ppm acetone at varied operating temperatures ranging from 155 to 245 °C, as shown in Figure S2 (Supporting Information). The gas-sensing test

Table 2. O_C, O_V, O_L, and Co^{2+}/Co contents of CoTM and CoTM-C series composites.

Sample	O_C	O_V	O_L	Co^{2+}/Co
CoTM-C4	21.22%	23.06%	55.72%	42.37%
CoTM-C3	21.33%	24.77%	53.90%	50.45%
CoTM-C2	32.27%	39.84%	27.89%	54.27%
CoTM-C1	29.35%	31.87%	38.87%	46.78%
CoTM	18.28%	27.96%	53.76%	39.39%

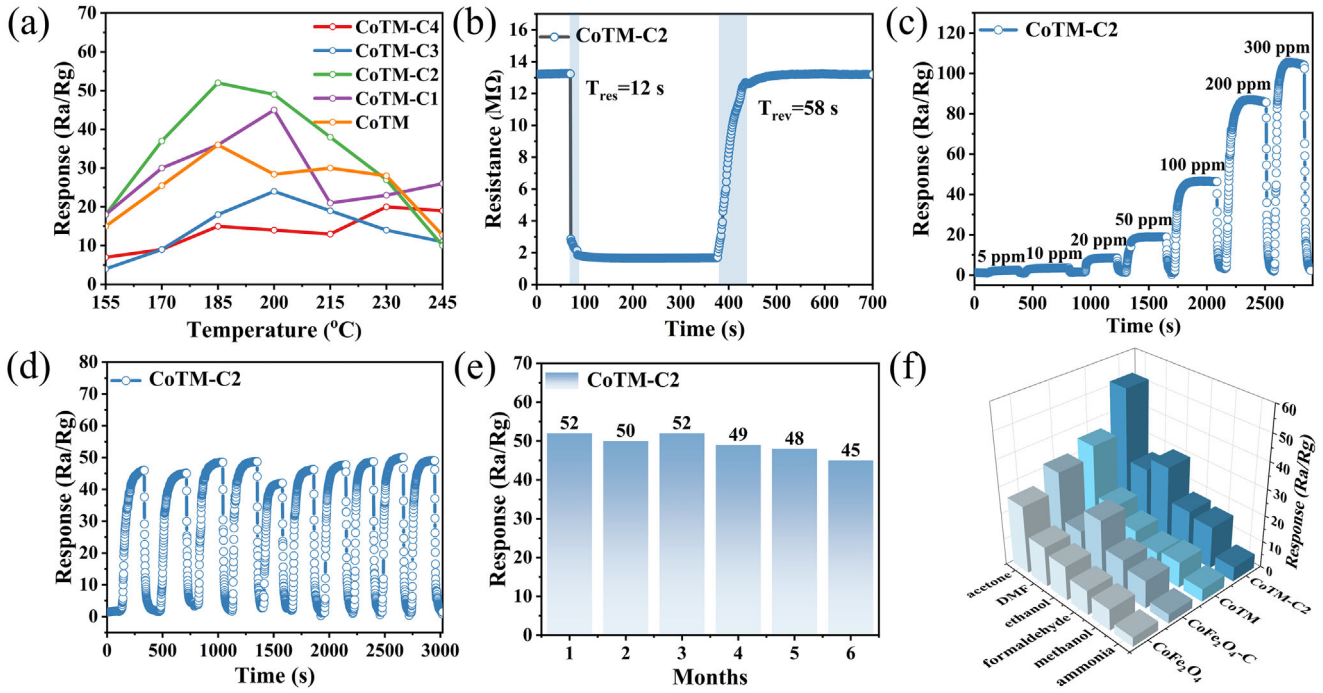

Figure 5. a) Sensing response of CoTM-C composites to 100 ppm acetone at varied operation temperatures from 155 to 245 °C; b) Response/recovery time of CoTM-C2 to 100 ppm acetone at 185 °C; c) Response of CoTM-C2 to varied concentrations of acetone at 185 °C; d) Stability of CoTM-C2 to 100 ppm acetone; e) Stability of response to acetone over six months; f) Selectivity columns of CoTM-C2 to acetone under the same concentration of interfering gases.

results demonstrate that $CoFe_2O_4$ modulated by TiO_2@MXene only or modulated by carbon reduction only shows enhanced gas response values compared to pristine $CoFe_2O_4$. However, the composite of $CoFe_2O_4$ modulated by two-step modulation, which are the incoporation of TiO_2@MXene and the carbon reduction consecutively on $CoFe_2O_4$, shows the optimal response to acetone compared to one-step modulation of $CoFe_2O_4$. The fitted XPS spectra of O 1s for $CoFe_2O_4$, CoTM, $CoFe_2O_4$-C, and CoTM-C2 samples are shown in Figure S3 (Supporting Information). The pristine $CoFe_2O_4$ sample (without any modulation) exhibits an oxygen vacancy concentration of 22.5%. In contrast, controlled variable experiments show that the CoTM sample, prepared by incorporation of TiO_2@MXene onto $CoFe_2O_4$, has an oxygen vacancy concentration of 27.96% presenting a 5.46% increase relative to the pristine $CoFe_2O_4$. Furthermore, the sample $CoFe_2O_4$ treated with the second-step carbon reduction modulation alone ($CoFe_2O_4$-C), exhibits an oxygen vacancy concentration of 29.19%, representing a 6.69% increase compared to pristine $CoFe_2O_4$. Furthermore, the pristine $CoFe_2O_4$ subjected to two-step modulation (CoTM-C2) involving the incorporation of TiO_2@MXene followed by carbon reduction displays a significantly higher oxygen vacancy concentration of 39.84%, corresponding to a 17.34% increase relative to $CoFe_2O_4$. Evidently, the combined processes of incorporating TiO_2@MXene and implementing carbon reduction on $CoFe_2O_4$ exert a synergistic effect in regulating oxygen vacancies.

Due to the CoTM-C2-based sensor exhibiting the highest response among all the composites, it was further evaluated for other gas-sensing performances. For instance, at 185 °C, the response/recovery times toward 100 ppm acetone are 17 s/54 s, as illustrated in Figure 5b. This represents reductions of 35 s/100 s, respectively, compared to the pristine $CoFe_2O_4$ (Figure S4, Supporting Information). Figure 5c shows the dynamic response of CoTM-C2 sensor upon exposure to 5–300 ppm acetone at 185 °C. It can be seen that the sensor has a strong dynamic response recovery characteristic to acetone, and the response value increases with increasing acetone concentration. To assess the stability of the CoTM-C2 composite, thermogravimetric analysis (TGA) was performed, as depicted in Figure S5 (Supporting Information). The results show that the material undergoes only a 9.50% mass loss when heated to 400 °C at a heating rate of 2 °C min^{-1} in air. Notably, at the operating temperature of 185 °C, the mass loss is as low as 2.04%, indicating that only water is lost without structural changes. In addition, to further validate its long-term usage reliability, CoTM-C2 sensor was tested for 10 cycles at 185 °C (Figure 5d) and repeatedly tested against 100 ppm acetone over a 6-month period (Figure 5e), which both show minimal fluctuations in the response, demonstrating the good repeatability and long-term stability of CoTM-C2-based sensor. Selectivity is also an important indicator of a gas sensor's performance. The response sensitivities of CoTM-C2 sensor to 100 ppm ammonia, formaldehyde, methanol, ethanol, and Dimethylfumarate (DMF) at 185 °C are shown in Figure 5f. The sensor shows a higher response value for acetone compared to the other interfering gases, demonstrating its excellent selectivity. In the actual use of the acetone sensor, humidity may also affect the response of the sensor. Therefore, the humidity response of the CoTM-C2 sensor was tested in the humidity range of 25% RH (relative humidity)-75% RH at 185 °C (Figure S6a, Supporting Information). As demonstrated in Figure S6a (Supporting Information), the sensor shows

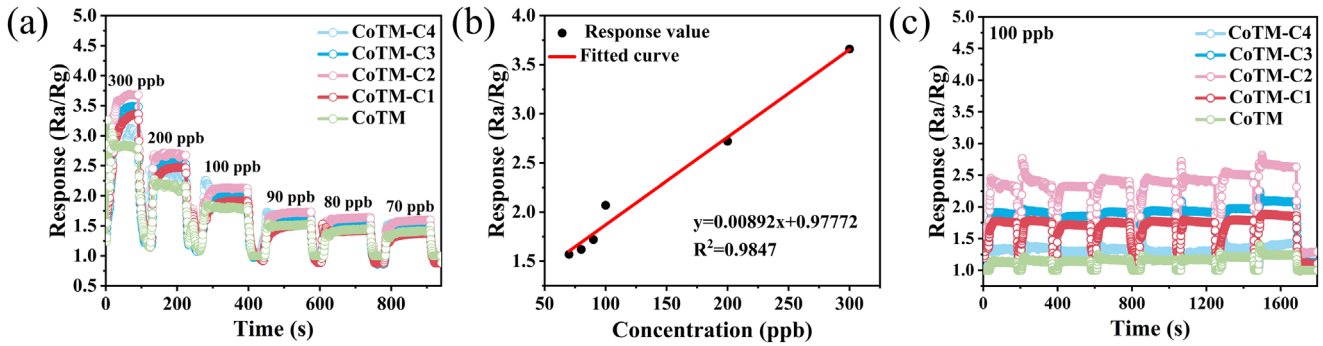

Figure 6. a) Response/recovery curves for varied acetone gas concentrations (70–300 ppb); b) Response-concentration linear fit curve for CoTM and CoTM-C series composites; c) Dynamic cycling curves of CoTM and CoTM-C composites to 100 ppb acetone.

an excellent humidity resistance at an operating temperature of 185 °C. The response of the sensor CoTM-C2 to 100 ppm acetone at different humidity at 185 °C is shown in Figure S6b (Supporting Information). The sensitivity of the sensor in an acetone atmosphere decreases considerably with the increase of ambient humidity. This phenomenon can be attributed to the fact that the water molecules adsorbed on the surface of the CoTM-C2 composites form a barrier layer under high humidity conditions, which prevents the effective adsorption of acetone gas, thus leading to a decrease in the gas-sensitive performance. However, in a high humidity environment (e.g., 75% RH), the sensor still exhibits significant sensitivity to acetone (10–15), indicating that it can function normally even under high humidity conditions.

In addition, healthy individuals exhale acetone gas at concentrations of 0.3–0.9 ppm, while diabetic patients exhale acetone gas at concentrations as high as 0.9–25 ppm. Considering the utility of CoTM-C composites in the diagnosis of disease, the gas-sensitizing properties of the composites were further evaluated for acetone at ppb levels. As shown in **Figure 6a**, the sensor still shows a significant response to low concentrations of acetone (70–300 ppb). From the corresponding concentration-sensitivity linear fit curve (Figure 6b), it can be seen that the sensor response value is positively correlated with the increase in concentration, with a good linear fit and an R^2 of 0.9847. The 100 ppb acetone test of CoTM-C2-based sensor over 8 cycles is shown in Figure 6c, indicating that its sensitivity repeatability is good (2.6–100 ppb) and further verifying its stability and reliability in detecting acetone at ppb levels. Compared with other sensors reported in the literature (**Table 3**), the sensor developed in this study demonstrates significant advantages in key performance parameters such as high gas response value and low operating temperature, further validating the excellent sensing performance.

2.3. Sensing Mechanism

As a typical n-type semiconductor, the sensing behavior of $CoFe_2O_4$ can be explained by the space charge model. The fundamental sensing mechanism primarily involves three sequential surface processes: gas adsorption, redox reaction, and subsequent desorption. These processes collectively modulate the surface carrier concentration and spatial distribution of the electron depletion layer, thereby inducing measurable resistance variations in the sensing element.

$CoFe_2O_4$ first adsorbs oxygen molecules from the environment, which capture free electrons and ionize them into negative oxygen ions (O_2^-, O^-, or O^{2-}). This charge transfer process establishes an electron depletion layer (EDL) extending several nanometers from the surface, consequently elevating the baseline resistance by creating potential barriers at grain boundaries. When the sensor is exposed to a reducing gas environment such as acetone, the acetone molecules react with the oxygen ions adsorbed on the surface, releasing electrons back into the conduction band. This electron replenishment effect reduces the EDL thickness and the Schottky barrier height at interparticle contacts, ultimately decreasing the overall sensor resistance through

Table 3. The acetone sensing performances of materials in references and this work.

Materials	Concentration [ppm]	Temperature [°C]	Response
$CoFe_2O_4$ nanoparticles[31]	100	220	17.5
Porous $CoFe_2O_4$ nanorods[32]	500	350	56.8%
Ce doped $CoFe_2O_4$[33]	100	200	138%
$CoFe_2O_4$ nanostructure foams[34]	150	300	30%
Al-Doped ZnO[35]	10	300	13.41
NiO/SnO_2 [36]	50	300	20.18
CeO_2–SnO_2 nanosheets[37]	750	280	47
ZIF-8 derived ZnO@CeO_2[38]	100	210	32
This work	100	185	52

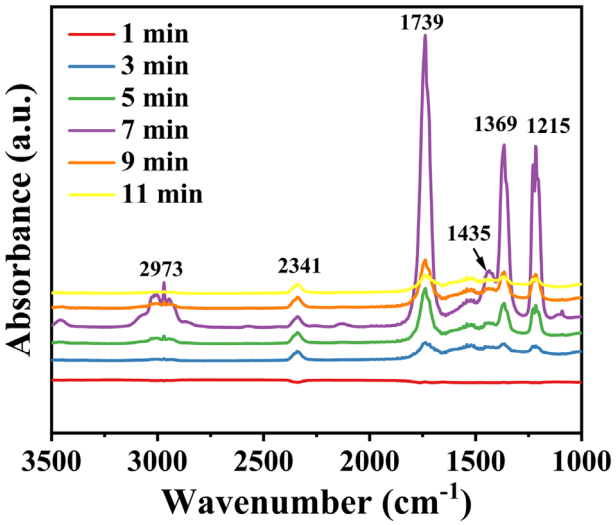

Figure 7. In situ DRIFT spectra of acetone absorption on CoTM-C2 at 185 °C.

improved charge carrier mobility. The reaction process on the $CoFe_2O_4$ surface can be roughly described by the following three equations:[39]

$$O_2\,(\text{gas}) \rightarrow O_2\,(\text{ads}) \quad (1)$$

$$O_2\,(\text{ads}) + e^- \rightarrow 2O^-\,(\text{ads}) \quad (2)$$

$$CH_3COCH_3\,(\text{ads}) + 8O^-\,(\text{ads}) \rightarrow 3CO_2\,(\text{gas}) + 3H_2O\,(\text{gas}) + 8e^- \quad (3)$$

To further explore the gas-sensing reaction mechanism, the in situ diffuse reflectance infrared Fourier transform spectroscopy (DRIFT) technique was employed to investigate the acetone sensing process on the surface of CoTM-C2 composite, with analysis of reaction intermediate evolution. As depicted in **Figure 7**, the IR spectra exhibit peak variations upon introducing acetone gas into the reaction chamber. The peaks at 1739 and 1215 cm^{-1} are assigned to the stretching vibrations of C═O and C—C bonds in acetone, respectively.[40] The 1369 cm^{-1} peak originates from acetone methyl groups formed via acetone dissociation, while the 1435 cm^{-1} peak suggests the formation of acetone dimers through condensation reactions.[41,42] Eventually, acetone undergoes oxidation to produce CO_2, evidenced by the peak at 2341 cm^{-1}. The emerging peak at 2973 cm^{-1} corresponds to —OH groups, likely resulting from the material absorbing H_2O molecules generated during the acetone reaction.

Compared with pure $CoFe_2O_4$, the acetone sensing performance of $CoFe_2O_4$-TiO_2@MXene and $CoFe_2O_4$-TiO_2@MXene-C composites is significantly improved, and the mechanism can be attributed to the multicomponent synergistic effect:

Firstly, MXene, a highly conductive 2D material, serves as an incorporation agent, which provides the abundant active sites and precisely regulates the concentration of oxygen vacancies at the interface between the metal oxide and MXene. Furthermore, Titanium in MXene undergoes partial oxidation during hydrothermal treatment. The in situ generated TiO_2 nanoparticles effectively prevent the restacking of MXene nanosheets, thereby fully utilizing their high specific surface area and excellent conductivity, which significantly enhances the gas diffusion and surface reaction kinetics. During the partial oxidation, the electrons are transferred from Ti^{3+} to oxygen molecules, resulting in Ti^{3+} being oxidized to Ti^{4+}. Concomitantly, oxygen reduction generates reactive O^{2-} species that coordinate with Ti^{4+}, while oxygen vacancies emerge as charge-compensation centers.[43] As demonstrated in Figure S3 (Supporting Information), the oxygen vacancy content of CoTM samples is higher than that of pristine $CoFe_2O_4$. Apparently, the incorporation of TiO_2@MXene on $CoFe_2O_4$ enables the modulation of oxygen vacancies. And the interfacial engineering between n-type $CoFe_2O_4$ and TiO_2 establishes n-n heterojunctions, inducing EDL reconstruction at phase boundaries. This heterojunction modulation synergistically enhances oxygen adsorption-activation cycles while optimizing charge carrier transport dynamics, ultimately amplifying the sensor's response magnitude. As shown in **Figure 8**, the work function of $CoFe_2O_4$ (4.80 eV) is higher than that of TiO_2 (4.46 eV), which results in the electron transfer at the interface from TiO_2 to $CoFe_2O_4$ until the Fermi energy levels reach equilibrium. This charge redistribution process induces a significant widening of the interfacial EDL, leading to a marked elevation in baseline resistance in the air environment.[44] When the CoTM-C sensor was in contact with acetone, the acetone molecules reacted with O^- to release electrons, forming a thin EDL between $CoFe_2O_4$ and TiO_2 to lower the potential barrier. Such interfacial band engineering effectively amplifies the sensor's response toward acetone through the enhanced surface electron depletion-recovery dynamics.

Second, the roles of carbon might be deduced into two parts: a reduction agent to modulate the oxygen vacancies of $CoFe_2O_4$ and a trigger agent of the Co^{3+}→Co^{2+} valence transition. Carbon reduction with glucose introduces oxygen vacancies into $CoFe_2O_4$, which not only provide additional adsorption sites and regulate the band structure but also optimize electrical conductivity and gas response. Moreover, the glucose-mediated hydrothermal reduction triggers the Co^{3+}→Co^{2+} valence transition, further generating charge-compensating oxygen vacancies in the lattice.[45] The large radius of Co^{2+} ions generates significant lattice stresses when they occupy lattice positions, triggering local structural distortions. This structural distortion destabilizes the coordination of oxygen ions by reducing the lattice binding energy, thereby lowering the energy barrier for oxygen desorption and facilitating the formation of oxygen vacancies. These oxygen vacancies serve as preferential adsorption sites that significantly accelerate gas adsorption/desorption kinetics through enhanced surface redox activity. As shown in Figure S3 (Supporting Information), the oxygen vacancy content of $CoFe_2O_4$ samples is enhanced after carbon reduction ($CoFe_2O_4$-C versus $CoFe_2O_4$). Similarly, the oxygen vacancy content of CoTM-C samples is also increased compared to CoTM, which indicates that the carbon reduction induces the formation of more oxygen vacancies.

Therefore, based on the foregoing discussions, it can be concluded that the two-step treatments involving TiO_2@MXene incorporation and carbon reduction act synergistically in regulating oxygen vacancies. The increased oxygen vacancies serve as adsorption centers to capture oxygen molecules and activate them into adsorbed oxygen species with higher reactivity, thereby strengthening the adsorption of acetone molecules and

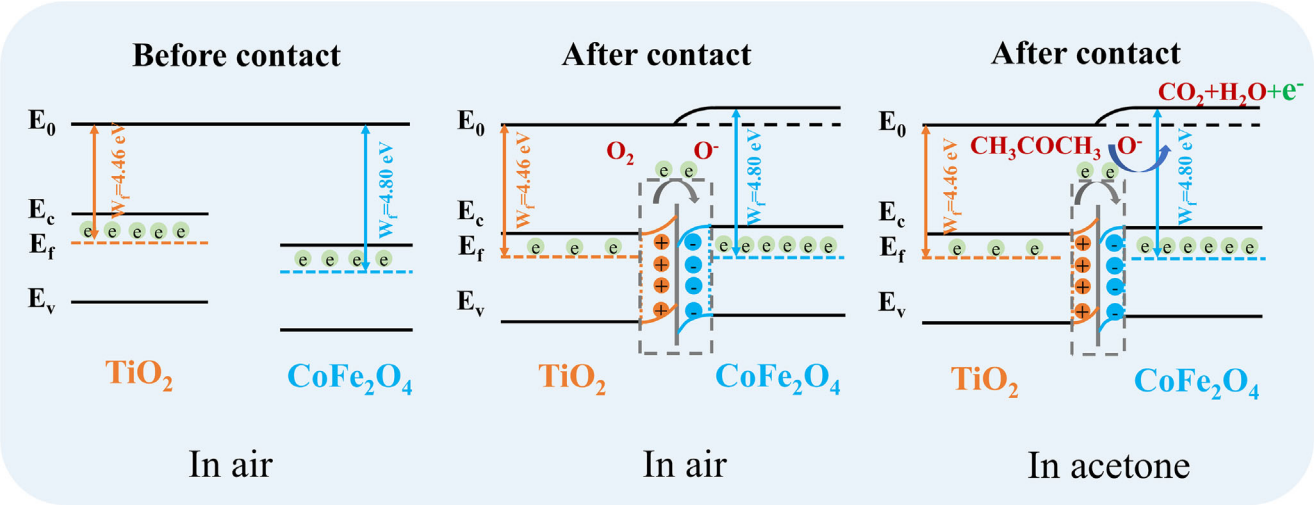

Figure 8. Schematic diagram of the energy band structure of the CoTM-C2 sensor.

facilitating acetone sensing. The accounts for the order of acetone sensing performances observed: $CoFe_2O_4$-TiO_2@MXene-C(CoTM-C) > $CoFe_2O_4$-TiO_2 @MXene(CoTM) > $CoFe_2O_4$.

3. Conclusion

This study innovatively proposes a two-step strategy (TiO_2@MXene doping and carbon reduction) to regulate oxygen vacancy concentration in $CoFe_2O_4$. MXene serves dual roles as a dopant and a titanium source to construct the $CoFe_2O_4$-TiO_2@MXene heterostructure, followed by glucose-derived carbonization to induce chemical reduction, successfully preparing $CoFe_2O_4$-TiO_2@MXene-C nanocomposites with tunable oxygen vacancies. By precisely controlling glucose content, the composite achieves gradient modulation of surface Co^{3+}/Co^{2+} ratio and oxygen vacancy concentration, resulting in superior acetone sensing performance. The optimized composite has fast response/recovery properties (17 s/54 s) to acetone gas with good long-term stability and excellent selectivity. The response value of 100 ppm acetone at 185 °C is as high as 52, which is 2.3 times higher than that of $CoFe_2O_4$. Especially for low concentrations of acetone still has a certain gas-sensitive response, with a detection limit of up to 70 ppb. The enhanced gas-sensing performance of this composite material can be attributed to the following oxygen vacancies modulations: the introduction of MXene coupled with the in situ growth of TiO_2 fabricates the heterojunction $CoFe_2O_4$-TiO_2@MXene, which effectively optimizes the distribution of oxygen vacancies; the glucose-assisted hydrothermal reduction process further enables the precise control over the concentration of oxygen vacancies. Moreover, the in situ formed TiO_2 effectively prevents MXene restacking, fully utilizing its high specific surface area and superior conductivity, thereby significantly improving gas diffusion kinetics. These findings offer a novel approach for designing high-performance acetone sensors and provide valuable insights into the mechanism by which gas-sensing performance is modulated by oxygen vacancies.

4. Experimental Section

Synthesis Process—Synthesis of Multilayer $Ti_3C_2T_x$ MXene Powders: First, LiF (0.5 g) was added to 20 mL of 12 M HCl (20 mL, 12 mol L^{-1}) at once and stirred magnetically for 5 min to form a mixed solution. Subsequently, Ti_3AlC_2 (0.5 g) powder was weighed and slowly added into the above mixture in ten portions within 30 min. After the addition, magnetic stirring was continued for 10 min and then transferred to a 60 °C water bath with magnetic stirring for 36 h to etch the Al layer in Ti_3AlC_2. After that, the obtained suspension was washed several times with de-watering centrifugation at 3500 rpm until the pH became neutral and then dried in a vacuum oven at 60 °C for 24 h. Finally, the dark $Ti_3C_2T_x$ powder was collected for further use.

Synthesis Process—Synthesis of $CoFe_2O_4$-TiO_2@MXene by In Situ Growth Method: Under sonication and magnetic stirring, $Co(CH_3COO)_2{\cdot}4H_2O$ (2 mmol) and $FeCl_3{\cdot}6H_2O$ (2 mmol), and an amount of MXene (n($Co(CH_3COO)_2{\cdot}4H_2O$): n(MXene) = 1:0.05–1:0.15) were dissolved in 1,2-propanediol (30 mL). The obtained solution was transferred to a Teflon-lined stainless-steel autoclave and kept at 180 °C for 24 h. After natural cooling to room temperature, the precipitate was obtained by centrifugation and washed with ethanol. Subsequently, the precipitate was roasted in air at 400 °C for 2 h at a ramp rate of 2 °C min^{-1} to obtain the $CoFe_2O_4$-TiO_2@MXene composite (hereinafter referred to as CoTM).

Synthesis Process—Synthesis of Carbon-Coated $CoFe_2O_4$-TiO_2@MXene: The synthesized $CoFe_2O_4$-TiO_2@MXene and a certain amount of glucose (feed mass ratio: 1:0.5–1:2) were dissolved in deionized water and stirred for 30 min, after which the obtained solution was transferred to a stainless-steel autoclave lined with Teflon and kept at 180 °C for 8 h. After cooling naturally to room temperature, the precipitates were obtained by centrifugation and washed with deionized water and dried overnight in an oven at 90 °C, to obtain a black powdered sample of $CoFe_2O_4$-TiO_2@MXene-C (abbreviated as CoTM-C). The samples were named CoTM-C1, CoTM-C2, CoTM-C3, and CoTM-C4 according to the amount of glucose added with the feed mass ratio of CoTM and glucose of 1/0.5, 1/1, 1/1.5, and 1/2, respectively.

Material Characterization: The crystal structure, physical phase combinations, and lattice parameters of the materials were investigated by X-ray powder diffractometer (XRD) (Ultima IV, Rigaku, Japan). The samples were analyzed by scanning electron microscopy (SEM) (Supra 55, Zeiss, Germany) and transmission electron microscopy (TEM) (JEM-2100F, JEOL, Japan) for microscopic morphology. The elemental and chemical states of the materials were analyzed using X-ray photoelectron spectroscopy (XPS) (Axis Supra, Shimadzu, Japan). The structure and

functional groups of the materials were analyzed using Fourier transform infrared (FT-IR) (TENSOR II, Bruker, Germany). The molecular structure and chemical bonding vibrations of the materials were analyzed by Raman spectroscopy (LabRAM Aramis, HORIBA Jobin Yvon S.A.S., France). The specific surface area and pore size of the materials were analyzed using a specific surface and porosity adsorption tester (BET) (ASAP-2460-4N, Micro, America). Gas-sensitive property tests were performed on a CGS-8 test system (Elite, China). The thermal stability of the material was characterized by thermogravimetric analysis (TGA) (STA7300, Hitachi, Japan). The contents of carbon, hydrogen, and oxygen in the samples were quantitatively determined using an elemental analyzer (EA) (vario MICRO cube, Elementary, Germany) with combustion-based methodology. The molecular structural variations of acetone during gas sensing were analyzed using in situ diffuse reflectance infrared Fourier transform spectroscopy (in situ DRIFT) (INVENIO-R, Bruker, Germany).

Detailed In Situ DRIFT Measurements: The sample was purged in argon at 185 °C for 30 min to remove surface impurities and environmental moisture. Subsequently, a background spectrum was collected under continuous argon flow. To establish an acetone atmosphere in the in situ cell, an acetone solution was introduced into the system using argon as the carrier gas. In situ DRIFT spectra were then recorded at 185 °C at different time intervals. Finally, the acetone atmosphere was purged from the system.

Gas Sensing Performance Testing: Firstly, an appropriate amount of a sample was poured into a mortar and pestle, and a few drops of deionized water were added and ground until a viscous paste was formed. Subsequently, a paint pen was dipped into the sample and applied to a hollow ceramic tube, evenly coating the sample until it completely covered the entire ceramic tube. Then left it to dry naturally for a few minutes. The ceramic tube was soldered to the hexagonal base, and the Ni-Cr heating wire was passed through the hollow part inside of the ceramic tube and soldered to the center of the hexagonal base. The gas sensor was placed on an aging bench and aged for 24 h at 80 mA before being used for gas sensitivity testing.

The gas sensitivity performance test was performed in a CGS-8 test system. Initially, the gas sensor was placed within the chamber of the test system, and the equipped glass cover was securely closed. The heating system was then turned on, allowing for temperature regulation by adjusting the current flow. Before data acquisition began, the sensor's initial resistance was stabilized to a value denoted as Ra.

Prior to the injection of the liquid, the external heating button was activated. A specific volume of the liquid, converted to gas, was then introduced into the evaporating dish inside the chamber using a microsyringe. This liquid evaporated, forming a gas of a particular concentration, which caused the sensor's resistance to change until it stabilized at a value referred to as Rg. Once stabilization was achieved, the glass cover was removed, and the fan was turned on to introduce air, allowing the resistance to stabilize again. Data acquisition was subsequently halted, and the collected data was saved for further analysis.

Supporting Information

Supporting Information is available from the Wiley Online Library or from the author.

Acknowledgements

This work was supported by the National Natural Science Foundation of China (NSFC 52072022). Guangdong Basic and Applied Basic Research Foundation (2025A1515012116), Department of Science and Technology of Guangxi Province (No. AB25069461), Startup Foundation from SCNU, Guangdong Provincial Key Laboratory of Optical Information Materials and Technology (2023B1212060065), the 111 Project.

Conflict of Interest

The authors declare no conflict of interest.

Data Availability Statement

The data that support the findings of this study are available from the corresponding author upon reasonable request.

Keywords

$CoFe_2O_4$, hydrothermal reduction, oxygen vacancies, $Ti_3C_2T_x$

Received: April 28, 2025
Revised: July 1, 2025
Published online: July 22, 2025

[1] R. A. Potyrailo, *Chem. Rev.* **2016**, *116*, 11877.
[2] N. Alizadeh, H. Jamalabadi, F. Tavoli, *IEEE Sens. J.* **2020**, *20*, 5.
[3] S. Wei, Z. Li, K. Murugappan, Z. Li, M. Lysevych, K. Vora, H. H. Tan, C. Jagadish, B. I. Karawdeniya, C. J. Nolan, A. Tricoli, L. Fu, *Adv. Sci.* **2024**, *11*, 2309481.
[4] A. Verma, D. Yadav, S. Natesan, M. Gupta, B. Chandra Yadav, Y. K. Mishra, *Microchem. J.* **2024**, *201*, 110713.
[5] A. A. Baharuddin, B. C. Ang, A. S. M. A. Haseeb, Y. C. Wong, Y. H. Wong, *Mater. Sci. Semicond. Process.* **2019**, *103*, 104616.
[6] L. Zhang, M. Zhou, F. Meng, J. Bai, D. Wang, M. Tang, Z. Wu, *TrAC Trends Anal. Chem.* **2025**, *187*, 118213.
[7] Y. Shi, T. Liu, R. Hu, H. Xu, C. Yang, L. Yang, L. Feng, X. Jiang, *J. Mater. Chem. A* **2024**, *12*, 4770.
[8] K. Li, S. Chen, M. Li, L. Liu, Y. Li, F. Wang, *Int. J. Hydrogen Energy.* **2024**, *59*, 1287.
[9] Q. Ma, J. Chen, Y. Sun, N. luo, C. Kou, X. Wang, J. Xu, J. Xu, P. Hu, *Appl. Surf. Sci.* **2024**, *649*, 159108.
[10] Y. Wang, Y. Wang, M. Jian, Q. Jiang, X. Li, *Nano-Micro Lett.* **2024**, *16*, 209.
[11] D. Li, H. Liang, Y. Zhang, *Carbon* **2024**, *226*, 119205.
[12] J. Li, X. Chen, X. Zhu, Y. Jiang, X. Chang, S. Sun, *Chin. Chem. Lett.* **2024**, *35*, 108286.
[13] C. Qin, Z. Wei, X. Zhao, J. Sun, J. Cao, Y. Wang, *Sens. Actuators, B* **2025**, *429*, 137288.
[14] H. M. Kim, K. a. Y. Shin, A. Mirzaei, W. Oum, E. B. i. Kim, S. Moon, S. P. Bharath, S. S. Kim, H. W. Kim, *Sens. Actuators, B* **2024**, *412*, 135802.
[15] X. Xu, W. Ma, H. Jiang, X. Wang, W. Liu, M. Wang, G. Sun, N. Ma, S. Ma, J. Wang, G. Chang, *Sens. Actuators, B* **2025**, *422*, 136595.
[16] H. Zhang, J. Hu, M. Li, Z. Li, Y. Yuan, X. Yang, L. Guo, *Sens. Actuators, B* **2021**, *349*, 130734.
[17] D. Huang, H. Li, W. Liu, Y. Chen, W. Wang, X. i. Tan, M. Zhao, Q. Cheng, M. Yi, G. Han, G. Liu, *Sens. Actuators, B* **2023**, *383*, 133594.
[18] L. Tao, Z. Guo, K. Pang, Z. Zeng, C. Wang, L. Huang, G. Zhu, L. Duan, J. Yang, Q. Li, *Appl. Surf. Sci.* **2024**, *663*, 160140.
[19] J. Zheng, S. Liu, R. Li, M. Huang, *Mater. Sci. Semicond. Process.* **2024**, *181*, 108635.
[20] Y. Fang, Z. Liu, J. Han, Z. Jin, Y. Han, F. Wang, Y. Niu, Y. Wu, Y. Xu, *Adv. Energy Mater.* **2019**, *9*, 1803406.
[21] B. Swensson, M. Ek, D. G. Gray, *ACS Omega* **2018**, *3*, 9449.
[22] C. Wang, L.-L. Gu, S.-Y. Qiu, J. Gao, Y.-C. Zhang, K. e.-X. Wang, J. i.-J. Zou, P.-J. Zuo, X.-D. Zhu, *Appl. Catal. B Environ.* **2021**, *297*, 120452.
[23] H. Chuai, W. Huang, S. Zhang, *ACS Catal.* **2025**, *15*, 3882.
[24] C. Li, G. Li, H. Ouyang, J. Huang, X. Hou, *J. Alloys Compd.* **2018**, *741*, 323.
[25] G. He, Y. Wen, C. Ma, X. Li, L. Gao, Z. Sun, *Int. J. Hydr. Energy.* **2021**, *46*, 5369.
[26] S. Alonzo, R. Dahal, M. Ashie, B. Bastakoti, *Microsc. Microanal.* **2024**, *30*, ozae044.598.

[27] J. Wang, C. Wan, Q. i. Tang, J. Xu, N. Xu, S. Yu, X. Wang, H. Tian, *Ceram. Int.* **2023**, *49*, 12814.
[28] Y. Luo, T. Lu, S. Jin, K. Ye, S. Yu, X. Zhang, X. Wu, P. Ma, J. W. Tester, K. Wang, *J. Supercrit. Fluids.* **2024**, *210*, 106290.
[29] C. Ji, Y. Liu, Y. Li, X. Su, J. Xu, L. Lu, *J. Magn. Magn. Mater.* **2021**, *527*, 167776.
[30] L. Zhao, C. Yu, C. Xin, Y. Xing, Z. Wei, H. Zhang, T. Fei, S. Liu, T. Zhang, *Adv. Funct. Mater.* **2024**, *34*, 2314174.
[31] H.-J. Zhang, L.-Z. Liu, X.-R. Zhang, S. Zhang, F.-N. Meng, *J. Alloys Compd.* **2019**, *788*, 1103.
[32] D. Thi Thanh Le, N. D. H. Long, C. Thi Xuan, N. Van Toan, C. M. Hung, N. Van Duy, L. Thi Theu, V. A. n. Dinh, N. D. Hoa, *Sens. Actuators, B* **2023**, *379*, 133286.
[33] M. S. Khandekar, N. L. Tarwal, I. S. Mulla, S. S. Suryavanshi, *Ceram. Int.* **2014**, *40*, 447.
[34] R. Montahaei, H. R. Emamian, *Ceram. Int.* **2022**, *48*, 26629.
[35] G. Lee, J.-H. Sim, G. Oh, M. Won, S. P. Mantry, D.-S. Kim, *Processes* **2023**, *11*, 3390.
[36] J. Hu, J. Yang, W. Wang, Y. Xue, Y. Sun, P. Li, K. Lian, W. Zhang, L. Chen, J. Shi, Y. Chen, *Mater. Res. Bull.* **2018**, *102*, 294.
[37] Y. Chen, M. Zhou, Z. Dong, A. Natan, S. Chen, Y. Yang, X. i. Huang, Y. Yang, *Appl. Phys. A.* **2019**, *126*, 33.
[38] C.-N. Wang, M.-X. Peng, L.-J. Yue, X.-Y. Yang, Y.-H. Zhang, *Sens. Actuators A Phys.* **2022**, *342*, 113650.
[39] X. Liao, X. Liu, Y. Wu, L. Qian, Y. Chen, Y. Wang, Z. Wu, A. Huang, X. Liu, J. Luo, *Sens. Actuators, B* **2025**, *436*, 137733.
[40] L. Li, D. Hong, B. Liu, T. Su, X. Yang, L. Yue, W. Zhang, *Sens. Actuators, B* **2025**, *433*, 137451.
[41] Q. Jia, H. Ji, Y. Zhang, Y. Chen, X. Sun, Z. Jin, *J. Hazard Mater.* **2014**, *276*, 262.
[42] W. Guo, L. Huang, B. Zhao, X. Gao, Z. Fan, X. Liu, Y. He, J. Zhang, *Sens. Actuators, B* **2021**, *346*, 130524.
[43] D. Kuang, L. Wang, X. Guo, Y. She, B. Du, C. Liang, W. Qu, X. Sun, Z. Wu, W. Hu, Y. He, *J. Hazard Mater.* **2021**, *416*, 126171.
[44] S. Uma, M. K. Shobana, *Inorg. Chem. Commun.* **2024**, *160*, 111941.
[45] M. Dong, H. Hu, S. Ding, Y. Duan, C. Cui, *Mater. Technol.* **2022**, *37*, 3184.